

Thermal instability in X-ray photoionized media in active galactic nuclei: influence on the gas structure and spectral features

A. C. Gonçalves^{1,2}, S. Collin¹, A.-M. Dumont¹, and L. Chevallier^{1,3}

¹ LUTH, Observatoire de Paris, Section de Meudon, 5 Place Jules Janssen, 92195 Meudon Cedex, France
e-mail: anabela.goncalves@obspm.fr

² CAAUL, Observatório Astronómico de Lisboa, Tapada da Ajuda, 1349-018 Lisboa, Portugal

³ Nicolaus Copernicus Astronomical Center, Bartycka 18, 00-716 Warszawa, Poland

Received 21 July 2006 / Accepted 28 November 2006

ABSTRACT

Context. A photoionized gas in thermal equilibrium can display a thermal instability, with three or more solutions in the multi-branch region of the S-shape curve that gives the temperature versus the radiation-to-gas-pressure ratio. Many studies have been devoted to this curve and to its dependence on different parameters, always in the optically thin case.

Aims. The subject of our study is the thermal instability in optically thick, stratified media in total pressure equilibrium. We are also interested in comparing photoionization models issued from the hot and cold stable solutions with the currently used models, which are computed with an approximate, intermediate solution.

Methods. We developed a new algorithm that selects the hot/cold stable solution and therefrom computes a fully consistent photoionization model. We implemented it in the TITAN code and computed a set of models encompassing the range of conditions valid for the warm absorber in active galactic nuclei.

Results. We demonstrate that the thermal instability problem is quite different in thin and thick media. Models computed with the hot/cold stable solution and with an intermediate solution differ throughout the gas slab, with the spectral distribution changing as the radiation progresses inside the ionized gas. These effects depend on the thickness of the medium and on its ionization.

Conclusions. This has observational implications for the emitted/absorbed spectra, ionization states, and variability. However impossible it is to know what solution the plasma will adopt when attaining the multi-solution regime, we expect the emitted/absorbed spectrum to be intermediate between those resulting from pure cold and hot models; such a phase-mixed medium can be reproduced well by intermediate solution models. Large spectral fluctuations corresponding to the onset of a cold/hot solution could be observed in timescales on the order of the dynamical time. A strong turbulence implying supersonic velocities should permanently exist in the multi-branch region of thick, stratified, pressure equilibrium media.

Key words. instabilities – radiation mechanisms: thermal – radiative transfer – methods: numerical – galaxies: active – X-rays: general

1. Introduction

It is well known that a photoionized gas in thermal equilibrium, i.e. a gas where the radiative heating is balanced by radiative cooling, can display a thermal instability (e.g., Krolik et al. 1981). The phenomenon manifests itself in the S-shape of the net cooling function¹ or, equivalently, through the curve giving the temperature versus the radiation-to-gas-pressure ratio. Such an S-shape curve allows for the co-existence of gas at different temperatures and densities for the same pressure ratio.

For a given value of the radiation-to-gas-pressure ratio, the gas can then be in three (or even more) states of thermal equilibrium that depend on the spectral energy distribution (SED) of the ionizing spectrum, on the abundances, and on other physical parameters affecting the heating and the cooling. One of these

states is thermally unstable, as it does not satisfy the stability criterion to isobaric perturbations (Field 1965):

$$\left(\frac{\partial \mathcal{L}}{\partial T}\right)_{P_{\text{gas}}} > 0, \quad (1)$$

where \mathcal{L} is the net cooling function, T the temperature, and P_{gas} the gas pressure. The two other states for which the derivative of \mathcal{L} is positive are stable. Such thermal instability is, for instance, at the origin of the two-phase model for the interstellar medium, where cold ($T \lesssim 300$ K) neutral atomic and molecular clouds are embedded in a warm ($T \sim 10^4$ K) intercloud medium (Field et al. 1969).

1.1. Optically thin media

Krolik et al. (1981) studied the thermal instability in the context of active galactic nuclei (AGN), for *optically thin*, X-ray illuminated gas. In such media, the radiation pressure keeps a constant value, and the energy balance equation solution depends only on the gas pressure. When the gas pressure is weak compared

¹ In this study, the net cooling function \mathcal{L} is defined as the difference between the cooling (Λ) and heating (Γ) functions in a given region and is expressed in units of $\text{erg cm}^3 \text{s}^{-1}$. It is also possible to use a net cooling function describing the energy balance per gram of material, per second.

to the radiation pressure, there is a unique, stable, “hot” solution, where both the heating and the cooling are dominated by Compton processes (Compton heating, inverse Compton cooling). As the gas pressure increases, atomic processes (photoionization heating, line and continuum cooling) become important, and multiple solutions arise. The harder the spectrum, the more extended the region encompassed by the multiple solutions. Then, above a given gas pressure, again a unique, but this time “cold”, solution arises. Krolik et al. show that multiple solutions may lead to the existence of a two-phase medium consisting of a hot, dilute gas confining denser, cooler clumps, which they identified as the broad line region (BLR) in AGN.

To better address the thermal instability issue, these authors introduced the ionization parameter Ξ (dimensionless), defined as

$$\Xi = \frac{F_{\text{ion}}}{n k T c}, \quad (2)$$

where F_{ion} is the incident ionizing flux between 1 and 10^3 Rydberg, n the total numerical density, and T the gas temperature. In a fully ionized gas, the radiation-to-gas-pressure ratio, $P_{\text{rad}}/P_{\text{gas}}$, is about equal to $\Xi/2.3$. The so-called S-shape curve is thus the curve giving T versus Ξ . Krolik et al. showed that the multi-branch region of this curve (or, equivalently, the multi-solution regime) corresponds to a range of Ξ between 1 and 10 for a typical AGN spectrum.

Since then, many studies have been devoted to the S-shape curve and to its dependence on the incident ionizing spectrum and on the abundances, but these were always for the *optically thin* case. The purpose of our study is different from previous works, as we are interested in *optically thick*² media such as the warm absorber (WA) in type 1 AGN, the X-ray line-emitting gas in type 2 AGN, or irradiated accretion discs in AGN and X-ray binaries. Our studies may be applied to media in any pressure equilibrium conditions, e.g., constant gas pressure, constant total³ pressure, or hydrostatic pressure equilibrium.

1.2. Optically thick media

Let us assume a medium in total pressure equilibrium, consisting of a slab of gas with a given density on the illuminated surface. Under these conditions, irradiation by X-rays induces a thermal instability beyond a given layer in the slab. The shape of the radiation spectrum and the radiation pressure itself depend on the considered position in the gas slab. Near the surface, the radiation spectrum is close to the incident spectrum irradiating the slab (close, yet different, owing to the additional presence of radiation returned by the non-illuminated side of the slab).

If the radiation-to-gas-pressure ratio is sufficiently large, the equilibrium temperature is high, and these layers are hot, displaying a unique, “hot” solution. This equilibrium temperature stays almost constant in the region. In deeper layers, two effects take place. First, the radiation spectrum is harder, owing to soft X-ray absorption by the previous layers; it contains only hard X-rays and diffuse ultraviolet radiation created within

the slab. As a consequence, the S-shape curve is more pronounced. Second, in the conditions of our models (described in Sect. 3), the radiation flux decreases – as does the radiation pressure – causing the gas to enter the multi-solution regime; the gas now has the choice between two stable solutions, a “hot” and a “cold” one. Finally, as the radiation penetrates still deeper into the slab, it suffers more and more modifications, and we get to a point where there is again a unique, “cold”, solution. The corresponding equilibrium temperature remains almost constant. This phenomenon can occur several times in the slab, according to the spectral distribution of the specific intensity through the medium. Each time the gas-phase changes, adjusting to a colder solution, the temperature profile displays a sharp drop by one order of magnitude or so. Between phase changes, the temperature remains more or less constant.

1.3. Electronic conductivity and alternative methods

One of the questions one may ask at this stage is “which solution to choose when there are two or more stable ones?” The answer depends on the previous history of the medium. A unique equilibrium state could be found if electron conduction were to be included (Begelman & McKee 1990; McKee & Begelman 1990; Różańska 1999). The well-known numerical difficulty linked to the thermal instability could be overcome using an integral formulation of the criterion giving the equilibrium solution, instead of a differential one (Różańska & Czerny 2000). However, coupling conductivity effects with a complete radiative transfer in photoionization models is a complicated task that has not yet been performed. Attempts to introduce electronic conduction are presently being undertaken by Chevallier et al. (in preparation).

There are, however, other methods to circumvent the problem of multiple stable solutions when dealing with photoionization codes. Two possibilities are discussed here. The first one was used to compute the vertical structure of irradiated accretion discs in hydrostatic equilibrium (e.g., Ko & Kallman 1994). This method consists in keeping the gas pressure constant during the iterations for convergence of the energy balance equation; this procedure is correct, but leads to a thermal instability, as described in the previous sections. Photoionization codes using this computational method (e.g. XSTAR: Kallman & Krolik 1995; Kallman & Bautista 2001) must then arbitrarily choose one of the stable solutions in the multi-branch region. The second possibility is to keep the density constant during the iterations for convergence of the energy balance equation, allowing the temperature value in the layer to be obtained; this computational method provides a unique solution, even if it is an approximate one, intermediate⁴ between the “cold” and the “hot” solutions present in the multi-branch region. This approach has been used in studies of the vertical structure of accretion discs (Raymond 1993; Shimura et al. 1995; Madej & Różańska 2000; Kawaguchi et al. 2001; Ballantyne et al. 2001).

Such a computational method is implemented in our photoionization code TITAN, described in the following section. It has been used in past years with good results; models computed with the “intermediate” temperature solution have been applied, for instance, to studies of the vertical disc structure with hydrostatic equilibrium (Różańska et al. 2002) and to total pressure equilibrium media (Różańska et al. 2002; Dumont et al. 2002; Różańska et al. 2006; Gonçalves et al. 2006; Chevallier et al. 2006). Since then, we have implemented a new algorithm in the

² Note that by “optically thick”, we here mean media optically thick to the photoionization continuum; this is the case for gas irradiated by a continuum that gets absorbed at one or more ionization edges, being therefore altered when passing through the medium. In a weakly ionized medium, this can occur for a column density as small as 10^{18} cm⁻².

³ In this paper, the total pressure includes the gas and radiation pressure, only; however, it should be possible to include other contributions, like a turbulent and/or a magnetic pressure component to the total pressure.

⁴ This “intermediate” solution should not be identified with the unstable solution (for which the derivative of \mathcal{L} is negative); it is simply a numerical alternative, intermediate between the stable solutions.

TITAN code. Here, we report on this new addition and its applications. In summary, the new algorithm allows us to choose between the “hot” or the “cold” stable solutions in the multi-branch region and then to compute a fully consistent model using the chosen solution. For the first time, it is thus possible to compare models issued from the true stable solutions with the approximate solution model and to estimate the degree of uncertainty of such an “intermediate” solution. Our improved version of the TITAN code will allow us to better understand the behavior of both kinds of computational schemes and to estimate their influence on the description of the ionized gas structure and on the modelled spectra emitted and absorbed by the medium.

In Sect. 2 we give a brief description of the TITAN code and discuss the different computational methods used in more detail. The models are described in Sect. 3. Section 4 contains a comparative study of the “hot”, “cold”, and “intermediate” solutions. In Sect. 5 we discuss some observational implications, and in Sect. 6 we summarize our conclusions.

2. Computational issues

2.1. The TITAN code

All our models, summarized in Table 1, were computed using the TITAN code. TITAN is a transfer-photoionization code developed by our team to correctly model optically thick (Thomson optical depth up to several tens) ionized media; it can be applied equally to thinner media (Thomson depth ~ 0.001 to 0.1 , e.g., Collin et al. 2004; Gonçalves et al. 2006). The code includes all relevant physical processes (e.g., photoionization, radiative and dielectronic recombination, fluorescence and Auger processes, collisional ionization, radiative and collisional excitation/de-excitation, etc.) and all induced processes. It solves the ionization equilibrium of all the ion species of each element⁵, the thermal equilibrium, the statistical equilibrium of all the levels of each ion, and the transfer of both the lines and the continuum. As output, it gives the ionization, density, and temperature structures, as well as the reflected, outward, and transmitted spectra. The energy balance is ensured locally with a precision of 0.01% , and globally with a precision of 1% .

TITAN is based on an idea initially depicted in Collin-Souffrin & Dumont (1986), and its conception took several years, the code being described for the first time in Dumont et al. (2000). It has been permanently upgraded since then, with some of the improvements described in, e.g., Dumont & Collin (2001), Dumont et al. (2002), and Chevallier et al. (2006). In particular, our code uses the accelerated lambda iteration (ALI) method, which allows for the exact treatment of the transfer of both the continuum and the lines (see Dumont et al. 2003, for a description of the ALI method applied to the modelling of the X-ray spectra of AGN and X-ray binaries). This is a major improvement over other photoionization codes such as Cloudy (Ferland et al. 1998), XSTAR (Kallman & Krolik 1995; Kallman & Bautista 2001), or ION (Netzer 1993, 1996) that use, at least for the lines, an integral formalism called the “escape probability approximation”. While ALI computes line and continuum fluxes very precisely by treating them in a consistent way, in approximate methods the computation of the absorption and emission lines is uncoupled. Furthermore, ALI enables a multi-direction utilization of the code, allowing for any illumination angle (including the normal direction) and any direction of the outward and

Table 1. Models computed with TITAN in the framework of this study. In the first column, the model name regroups information on the ionization (H: high, M: medium, L: low) and on the chosen computational solution (C: cold, H: hot, I: intermediate). The ionization parameter and column density values are given in Cols. 2 and 3, respectively. Column 4 lists the thermal instability solution chosen.

Model name	$\xi = L/n_H R^2$ (erg cm s ⁻¹)	N_H (cm ⁻²)	Thermal instability solution
HI 1_C	10 000	2×10^{23}	cold
HI 1_H	10 000	2×10^{23}	hot
HI 1_I	10 000	2×10^{23}	intermediate
MI 1_C	1000	2×10^{23}	cold
MI 1_H	1000	2×10^{23}	hot
MI 1_I	1000	2×10^{23}	intermediate
MI 2_C	1000	2.5×10^{23}	cold
MI 2_H	1000	2.5×10^{23}	hot
MI 2_I	1000	2.5×10^{23}	intermediate
MI 3_C	1000	3×10^{23}	cold
MI 3_H	1000	3×10^{23}	hot
MI 3_I	1000	3×10^{23}	intermediate
LI 1_C	300	5×10^{22}	cold
LI 1_H	300	5×10^{22}	hot
LI 1_I	300	5×10^{22}	intermediate
LI 2_C	300	8.5×10^{22}	cold
LI 2_H	300	8.5×10^{22}	hot
LI 2_I	300	8.5×10^{22}	intermediate

reflected emission. This fully operational version of the code offers the possibility of modelling an ionized medium in constant density, constant gas pressure, or constant total (i.e. gas plus radiation) pressure. It has recently been used to study the soft X-ray spectra of AGN (Chevallier et al. 2006) and applied to model real data as, for instance, the warm absorber in NGC 3783 with a single medium in total pressure equilibrium (Gonçalves et al. 2006), or the spectra of bright ultraluminous X-ray sources (Gonçalves & Soria 2006).

2.2. Different computational methods used

We recall that the set of equations describing the physical state of the gas (i.e. the local balance between the ionization and recombination processes, the excitations and de-excitations, as well as the local energy balance) is computed at each depth in the gas slab. In TITAN’s previous computational scheme, the thermal energy balance equation was solved for a given density at a given depth (that of the previous iteration); this method provides a unique solution for the temperature. The model corresponding to this scheme will be called the “intermediate” model hereafter.

In the new version of TITAN, the energy balance equation is solved for a given total pressure, assumed to be constant along the slab. In some regions of the cloud, this computational scheme leads to two stable solutions, described by two separate models. In one of the models, the “hot” solution is systematically chosen for all layers, while in the other model the “cold” solution is systematically preferred. These models will be called hereafter the “hot” and “cold” models, respectively. They actually represent two extreme results corresponding to a given gas composition and photoionizing flux, since they are compatible with the two stable solutions. It is important to stress that *these models differ not only in the layers where multiple solutions are possible, but also throughout the gas slab*, this because the entire radiation field will be modified in a thick medium.

⁵ Our atomic data include $\sim 10^3$ lines from ions and atoms of H, He, C, N, O, Ne, Mg, Si, S, and Fe.

This, and other behaviors of a slab of optically thick gas in constant pressure equilibrium, will be discussed in the following sections. We have chosen to work with a few models encompassing the range of conditions valid for the warm absorber in AGN, given in Table 1. The same study could, of course, be performed for a different set of values, but this would not change our main results and conclusions.

3. The models

All the models presented here were treated in a 1-D plane-parallel geometry, as slabs of gas illuminated from one side by a radiation field concentrated in a very small, pencil-like shape, centered on the normal direction. The resulting spectrum, reprocessed by the gas, is a combination of “reflection” from the illuminated side of the medium (not a real reflection, as it includes atomic and Compton reprocessing), “outward emission” (coming from the non-illuminated side of the medium), and a “transmitted” fraction of the incident ionizing continuum. The absorption spectrum (which corresponds to the outward emission in the normal direction) depends strongly on the column density, since the cool absorbing layers are located at the back side of the gas slab. The relative contribution of each component to the observed spectrum depends on parameters such as the size, the density, and the geometry of the ionized medium.

Our models are globally parameterized by the column density N_{H} (in units of cm^{-2}), the hydrogen number density at the illuminated side of the slab n_{H} (in units of cm^{-3}), the incident flux and SED, and the ionization parameter. This parameter is defined differently among authors and in this article, we use the ξ form of the ionization parameter, where

$$\xi = \frac{L}{n_{\text{H}} R^2} \quad (\text{in units of } \text{erg cm s}^{-1}) \quad (3)$$

in which R is the distance between the radiating source and the photoionized medium, and L is the source’s bolometric luminosity (in erg s^{-1}). In the following, we integrate L over the range $10\text{--}10^5$ eV, but some authors prefer to give ξ with L integrated over the $1\text{--}1000$ Ryd region, as used by XSTAR. Appropriate conversions should thus be applied if using different forms of the ionization parameter, and before any numerical comparison. Note that ξ , as well as n_{H} , are quantities defined at the illuminated surface of the slab. We recall that the hydrogen number density in constant pressure models varies along the slab, displaying a profile varying inversely with the temperature; also the spectral distribution of the ionizing radiation changes across the slab for media in pressure equilibrium, as for those discussed in this paper.

All our models were computed under total (i.e., gas plus radiation) pressure equilibrium, neglecting all other forms of pressure (e.g., turbulent, magnetic, etc.) contributing to the total pressure. The gas slabs were assumed to have cosmic abundances (Allen 1973) and the hydrogen numerical density at the illuminated surface was set to 10^7 cm^{-3} . Note that n_{H} is a minor parameter in this study, the overall spectrum being only proportional for values varying from 10^7 to 10^{12} cm^{-3} (this is usually the case, provided the ionizing spectrum is relatively flat); only the relative intensities of the forbidden and permitted emission lines (e.g., from He-like ions like O VII) are sensitive to changes in the density.

We simplified our models by assuming a null turbulent velocity component, but then micro-turbulence has little influence on the thermal and ionization structure for high column densities, where the cooling is dominated by bound-free transitions.

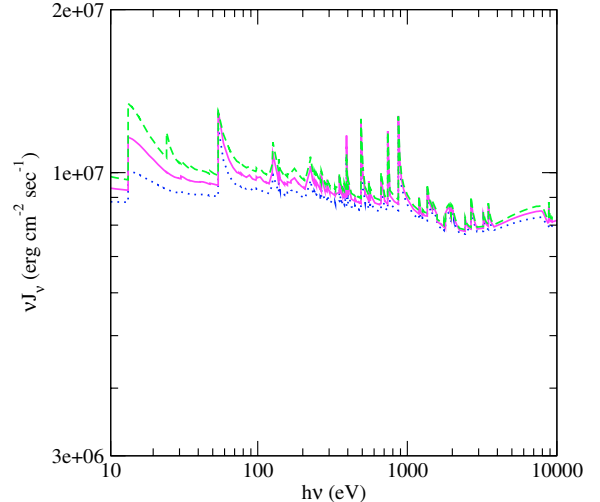


Fig. 1. This figure displays the spectral distribution of the mean continuum intensity, computed at the illuminated surface of the slab, for three “intermediate” models: MI 1_I (dotted line), MI 2_I (solid line), and MI 3_I (dashed line). For the sake of clarity, the spectral lines have been suppressed from this figure, where only the continuum is shown; this displays important discontinuities that increase with the slab thickness.

The thermal and ionization structures are mainly determined by the ionization parameter and the shape of the ionizing continuum. All the models in this paper assume an incident continuum described by a power-law of photon index $\Gamma = 2$, covering the $10\text{--}10^5$ eV energy range.

4. “Hot”, “cold”, and “intermediate” solutions

In this section, we illustrate the differences between the previously discussed computational methods by comparing the results obtained with the “hot”, “cold”, and “intermediate” models.

4.1. Behavior at the surface level

It is often assumed that the thermal instability problem in thick media is exactly the same as in thin media. This is not true, mainly for two reasons. First, the spectral distribution of the mean intensity J_{ν} at the illuminated surface of the slab is different from the incident spectrum, as it equally contains a “returning” radiation component emitted by the slab itself. As an illustration, Fig. 1 shows the spectral distribution of the mean continuum intensity at the slab surface for three “intermediate” models with $\xi = 1000$ and 3 different values of the column density. For the sake of clarity, the spectral lines were suppressed from the figure, and only the continuum is shown. We observe that the spectrum *on the surface* contains strong discontinuities, whose amplitude increases with the slab thickness. More generally, the intensity of the whole spectrum is seen to increase with the slab thickness (an expected behavior since the radiation emitted by a thicker slab should be stronger). Second, the spectral distribution changes as the radiation progresses inside the medium. As a consequence, the shape of the S-curve also changes, and instead of travelling along a given S-curve as $P_{\text{rad}}/P_{\text{gas}}$ decreases, the temperature follows successively different curves. This behavior is illustrated by the MI 1_I model in Fig. 2, which shows the spectral distribution of the mean continuum for two layers located at different depths in the gas slab

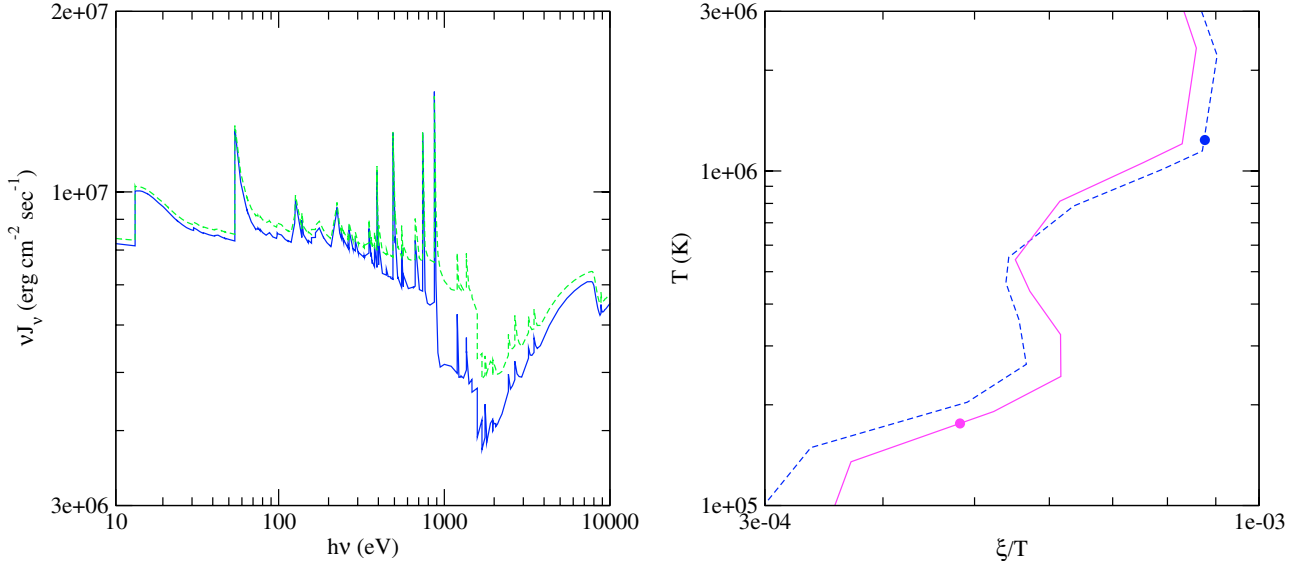


Fig. 2. This figure displays some results for an “intermediate” model with $\xi = 1000$ and $N_{\text{H}} = 2 \times 10^{23} \text{ cm}^{-2}$ (MI 1_I). In the *left-hand panel* we give the spectral distribution of the mean continuum for two layers located at different depths in the gas slab; these layers correspond to a column density value of 1.66×10^{23} (dashed line) and 1.90×10^{23} (solid line). In the *right-hand panel*, we display the S-curves giving T versus ξ/T for the same two layers (the same line-codes apply); the dots represent the equilibrium temperature found for each layer.

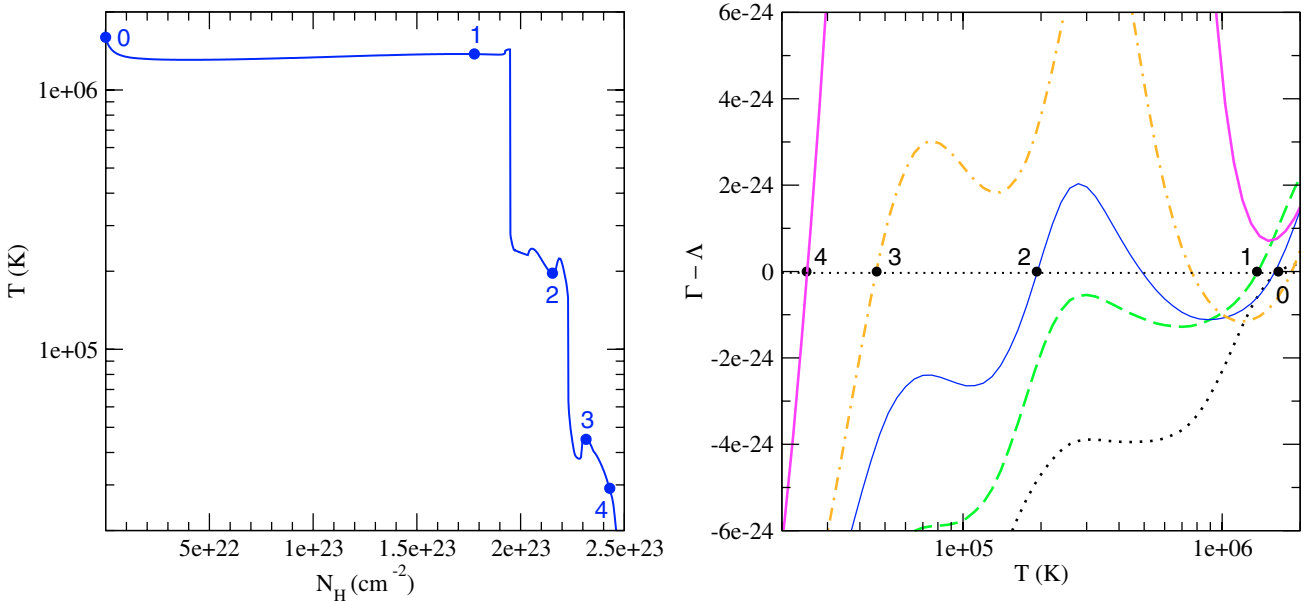


Fig. 3. In the *left-hand panel* we give the temperature profile along the slab (i.e., versus the column density) for the model MI 2 ($\xi = 1000$, $N_{\text{H}} = 2.5 \times 10^{23}$) computed with the “cold” solution. The dots represent gas at different depths in the slab, for which we have plotted the corresponding cooling curves in the right-hand panel. We observe that the net cooling function \mathcal{L} has one single solution for the layers labelled 0, 1, and 4 in the slab, while there are three possible solutions for the layers labelled 2 and 3; from these, only the “cold” solution was selected to compute the gas structure and spectra.

(left-hand panel) and the corresponding curves giving T versus ξ/T (right-hand panel), which is the same as representing the usual S-shape curve. We can see that the S-curves are different for the two represented layers and, in particular, that the curve corresponding to the deeper layer displays a larger multi-branch region, which is due to its larger absorption trough.

4.2. Comparison between cooling curves

Figures 3–5 concern a slab of gas with a total column density equal to $2.5 \times 10^{23} \text{ cm}^{-2}$, ionized by an incident continuum

with $\xi = 1000$ (MI 2 model). These figures display, respectively for the “cold”, “hot”, and “intermediate” solution models, the temperature profile versus the column density (left-hand panel) and the net cooling function ($\mathcal{L} = \Lambda - \Gamma$) versus the temperature, at different depths in the gas slab (right-hand panel); the various layers represented here have been marked and labelled in the left-hand panel. By comparing both plots we can verify that \mathcal{L} cancels for the equilibrium temperatures observed in the gas structure.

We recall that the cooling curves of the “hot” and “cold” models are determined for a given total pressure, while those of the “intermediate” models are computed for a given density. We

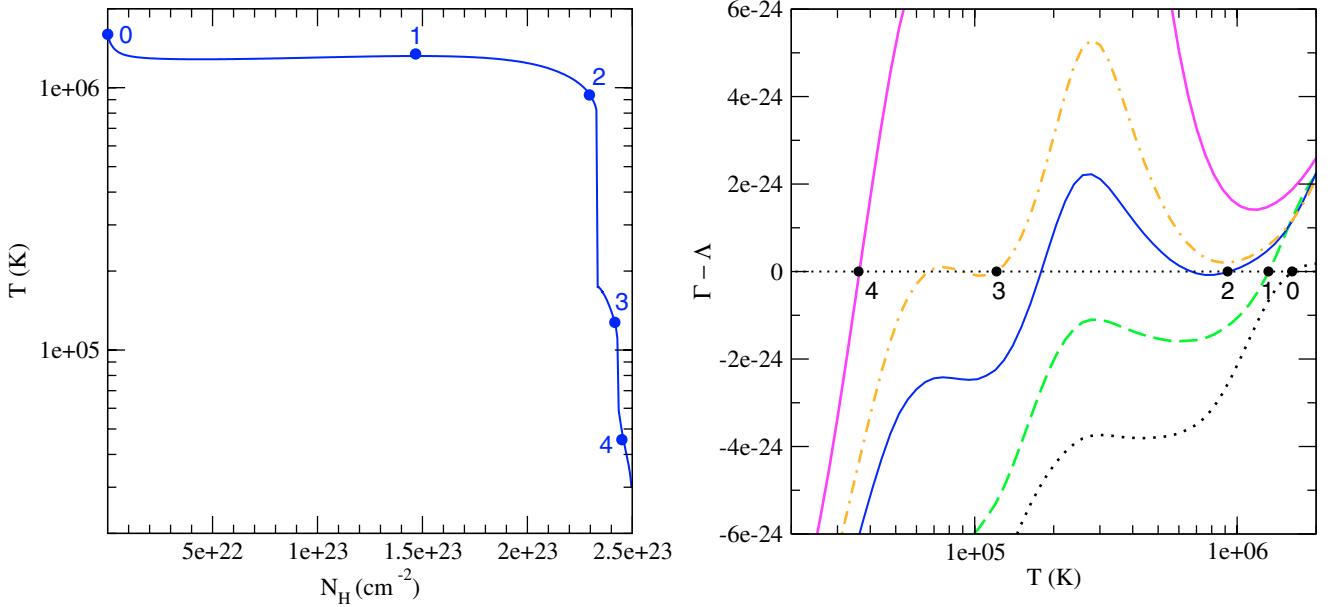


Fig. 4. Same as in Fig. 3, except the model has been computed with the “hot” solution. In the right-hand panel, layers labelled 2 and 3 display three possible solutions, from which the “hot” one has been systematically chosen; the layers labelled 0, 1, and 4 display a single solution.

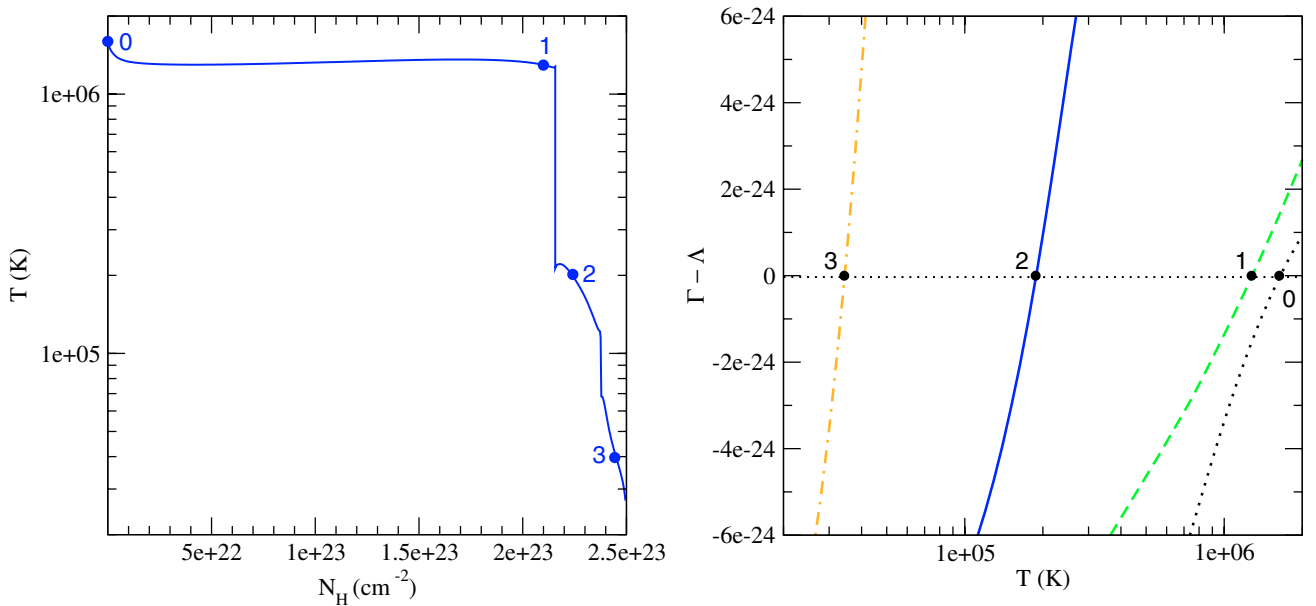


Fig. 5. Same as in Figs. 3 and 4, except the model has been computed with the “intermediate” solution. In this case, the cooling curves in the *right-hand panel* always provide a unique solution, independently of the depth of the layer considered (dots on the *left-hand panel*).

can check that the isobaric cooling curves of the “cold” and “hot” models (Figs. 3 and 4, respectively) display three solutions for $\mathcal{L} = 0$, while the isodensity cooling curves of the “intermediate” model (Fig. 5) always show a unique solution. We stress that it is impossible to compare the cooling curves in exactly the same conditions, as the models computed with these three solutions differ considerably. Indeed, the radiation field is completely different in the three models, even at the illuminated surface layer; therefore, the isobaric cooling curves differ strongly, even for a layer located at a similar depth in the gas slab.

Let us first examine the cooling curves corresponding to the “cold” model (Fig. 3). We can see that there is a unique solution at the illuminated surface and at position 1, while at positions 2 and 3 there are three possible solutions, from which the coldest one is chosen. Near the back surface of the slab, at

position 4, the solution is again unique. Similarly, for the “hot” model (Fig. 4), the solution is unique at the surface and at position 1, but at positions 2 and 3 the curve has three solutions, from which the hotter one is chosen. Then, the solution is again unique at position 4. However, the multi-branch region is different in the case of the “hot” or the “cold” models, which shows how much these two models differ. Finally, in the case of the “intermediate” model (Fig. 5), all solutions are unique. Given these differences, we would expect that the previous computational scheme used by TITAN, with its isodensity cooling curves, would be completely wrong, but this is not the case, as we will see later on. Indeed, such a method provides temperature structures and spectra that are intermediate between those of the “cold” and the “hot” models.

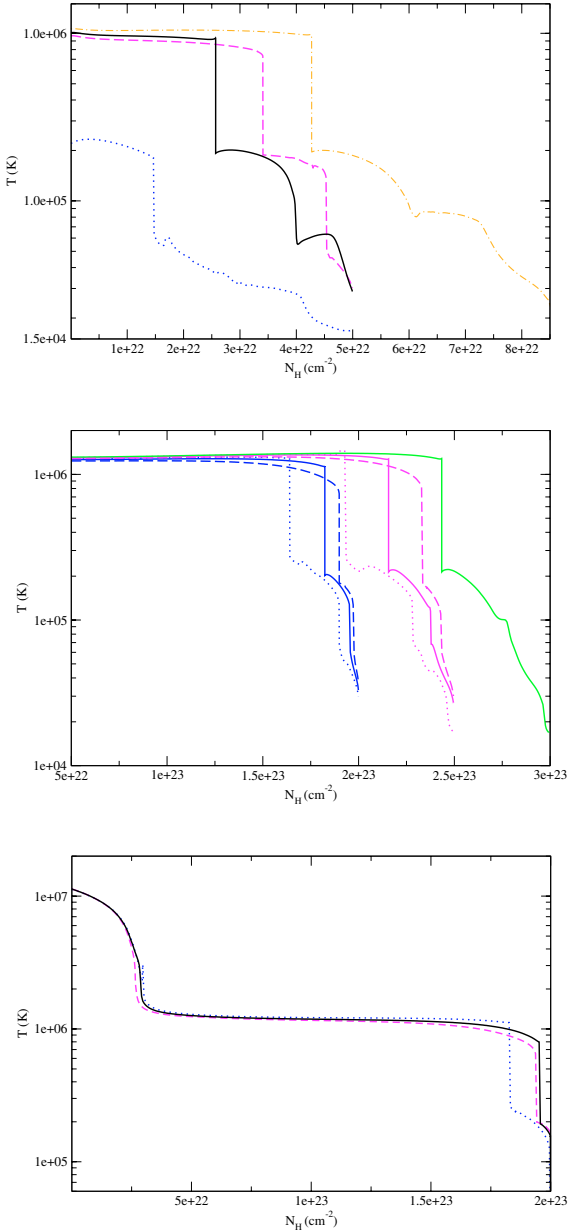


Fig. 6. Temperature profiles versus the column density for a set of models with different ξ and N_H . In the *top panel*, the LI 1 models (dashed line: “hot” solution; dotted line: “cold” solution; solid line: “intermediate” solution); for comparison, we also plotted the LI 2_I model (dashed-dotted line). In the *middle panel*, several MI models for different values of the column density (dashed lines: “hot” solution models; dotted lines: “cold” solution models; solid lines: “intermediate” solution models). Finally, in the *bottom panel*, the HI 1 models (the same line-codes apply).

4.3. Temperature profiles

Figure 6 displays the temperature profiles for the “cold”, “hot”, and “intermediate” solutions, for a set of LI ($\xi = 300$), MI ($\xi = 1000$), and HI ($\xi = 10000$) models. By analyzing the figure, two results appear clearly:

- first, the differences between the “hot”, “cold”, and “intermediate” models increase as ξ decreases;
- second, the temperature always decreases strongly near the non-illuminated surface of the slab, whatever the column density.

In the following, we present some clues that help for understanding these behaviors.

4.3.1. Influence of the ionization parameter

For the higher ionization models ($\xi = 10000$), the “hot”, “cold”, and “intermediate” solutions provide very similar results (cf. Fig. 6, bottom panel). The results are quite different for the lower ionization models ($\xi = 300$), since the first layer at the illuminated side of the slab is already in the multi-solution regime (cf. Fig. 6, top panel). In this case, since the “hot” and “cold” solutions correspond to very different equilibrium temperatures, there is also a large difference in the whole medium structure. This is illustrated by Fig. 7, which is similar to Figs. 3–5, except we now address the case of the LI 1 “cold” solution model. The figure shows that, already at the illuminated surface of the slab (labelled 0 in the left-hand panel), the net cooling curve cancels for three values of the temperature; this multi-solution regime lasts until the deeper position labelled 4 in the left-hand panel.

It is possible to address this situation and try to find an adequate explanation for the behavior of the LI 1 model by looking into what’s happening with the Ξ ionization parameter (or, which is similar, studying the $P_{\text{rad}}/P_{\text{gas}}$ ratio). Since the multi-solution regime occurs for a given range in Ξ , one expects that the associated region in the slab would correspond to layers where $P_{\text{rad}}/P_{\text{gas}}$ is on the order of a few units. This is indeed the case, as shown in Fig. 8, which displays the variation in P_{rad} , P_{gas} , and $P_{\text{rad}}/P_{\text{gas}}$ throughout the slab, for the “hot” and “cold” solutions of a set of LI, MI, and HI models. The radiation pressure due to the lines, $P_{\text{rad}}(\text{lines})$, is also shown, as this component can be quite important near the back side of the slab. Note that P_{rad} , also represented in the figure, already includes the contribution from $P_{\text{rad}}(\text{lines})$.

When observing Fig. 8, we first notice that, in all cases, the pressure is entirely dominated by P_{rad} , and that $P_{\text{rad}}/P_{\text{gas}}$ at the illuminated surface increases with ξ , as expected. The $P_{\text{rad}}/P_{\text{gas}}$ ratio decreases across the slab from the illuminated surface to the back side as the radiation is absorbed, with the slab entering the multi-solution regime when $P_{\text{rad}}/P_{\text{gas}}$ is on the order of 2.5; this is true whatever the pressure ratio at the illuminated side. It is easy to see that such a value was promptly attained in the case of the LI 1 model discussed before. As a consequence, we were already able to observe a “cold” and a “hot” solution at the surface of the slab.

It is also interesting to note that, in spite of a big difference in temperature, the gas pressure at the surface is almost the same for the “cold” and “hot” models. This behavior is actually due to an automatic adjustment of the density, which is equal to $5 \times 10^7 \text{ cm}^{-3}$ in the first layer of the “cold” model, instead of the lower initial value of 10^7 cm^{-3} . The figure also shows that, for all values of the ionization parameter, the pressures in the three models (“cold”, “hot”, and “intermediate”) are quite similar, except for $P_{\text{rad}}(\text{lines})$ near the back side of the slab. Indeed, the contribution from the lines is always lower in a hot medium than in a cold medium, which can emit intense ultraviolet lines. Therefore, the smaller the ionization parameter, the more important the lines. It is thus easy to understand how $P_{\text{rad}}(\text{lines})$ can even dominate the radiation pressure near the back side of the LI 1_C model (cf. Fig. 8, left-hand panel).

Note finally that the sharp temperature drops observed in the left-hand panel of Figs. 3–5, and 7 do not occur exactly at the same value of $P_{\text{rad}}/P_{\text{gas}}$ for all the models. This is due to the shape of the S-curve, and to the different spectral distributions inside the slab, which depend not only on the type of model

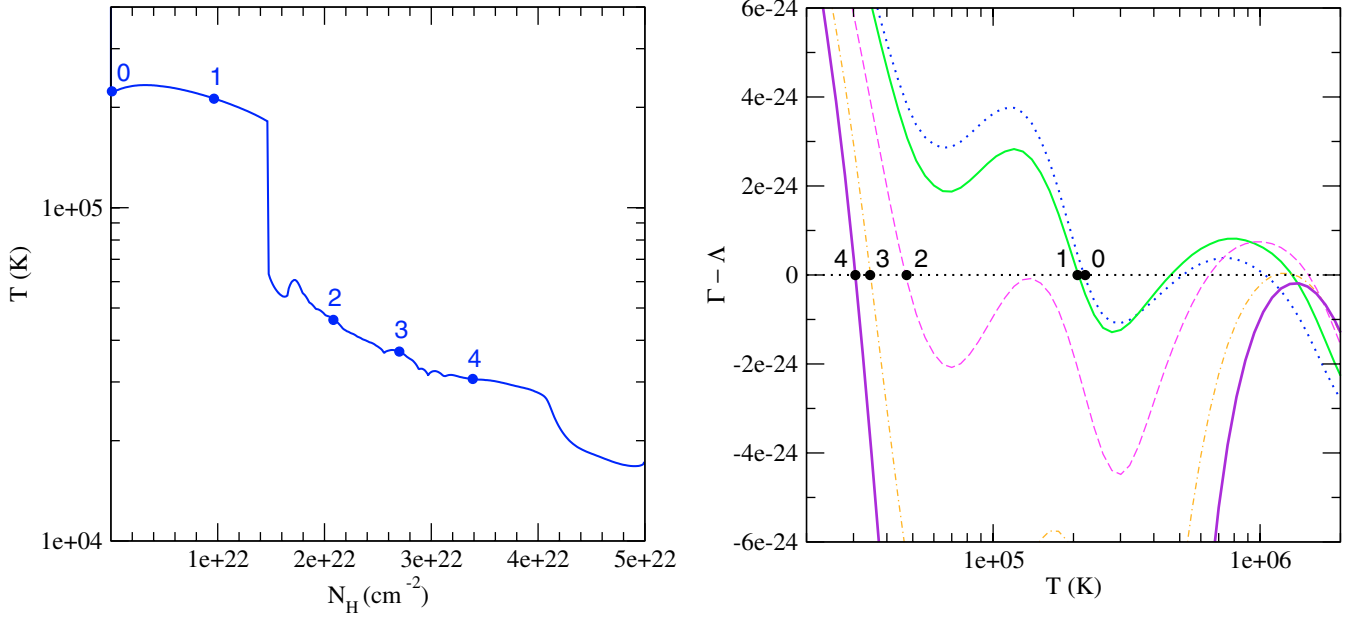


Fig. 7. Temperature profile versus the column density for a model with $\xi = 300$ and $N_{\text{H}} = 5 \times 10^{22}$ (*left-hand panel*). We have marked several layers, corresponding to different positions in the gas slab, labelled from 0 (at the illuminated surface) to 4 (deeper in the slab). In the *right-hand panel*, we give the corresponding cooling curves, which display one (position 4) or more solutions. It is interesting to note that, at such low ionizations, the surface layer is already in the multi-solution regime, displaying 3 possible solutions from which the coldest one has been chosen.

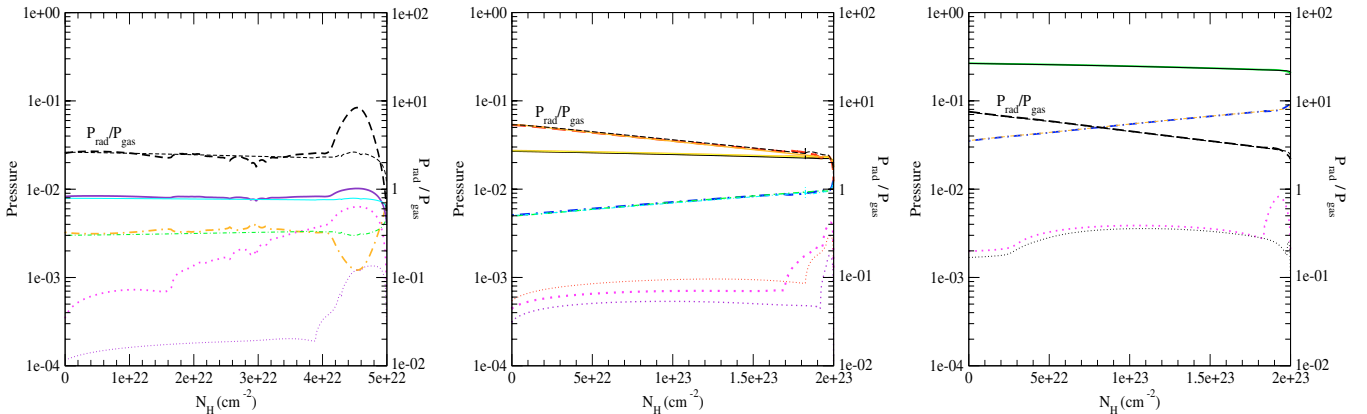


Fig. 8. This figure shows various pressure quantities computed with the “cold” (green, black, and violet thick lines), “hot” (blue, orange, and magenta thin lines), and “intermediate” (cyan, yellow, and red very thin lines) solutions for the models LI 1 (*left-hand panel*), MI 1 (*middle panel*), and HI 1 (*right-hand panel*). For the sake of clarity, the “intermediate” solution values are only shown for one of the models (MI 1, *middle panel*). In all the panels, P_{rad} is given in solid lines, P_{gas} in dashed-dotted lines, $P_{\text{rad}}(\text{lines})$ in dotted lines, and the $P_{\text{rad}}/P_{\text{gas}}$ ratio in dashed lines; also, the *left-hand y-axis* (10^{-4} –1) corresponds to the P_{rad} , P_{gas} , and $P_{\text{rad}}(\text{lines})$ values, while the *right-hand y-axis* (10^{-2} – 10^2) corresponds to the $P_{\text{rad}}/P_{\text{gas}}$ ratio.

(“cold” or “hot”), but also on the ionization parameter and on the total thickness of the medium.

4.3.2. Influence of the medium thickness

As already noted by Róžańska et al. (2006) and Chevallier et al. (2006), the thickness of a pressure equilibrium medium cannot exceed a maximum value for a given ionization parameter. This is explained by the fact that, when the temperature reaches low values (on the order of 10^4 K), the radiation pressure becomes dominated by the spectral lines, and therefore the gas enters a new multi-solution regime. When the temperature drops to the cold values corresponding to a molecular gas, we reach a limit and are unable to provide a solution, as our code cannot handle molecular gas.

If the maximum thickness of a medium in pressure equilibrium is a known issue, there are two other puzzling problems related to the thickness of the slab. The first is related to the fact that the temperature always decreases rapidly near the non-illuminated side of the gas slab. The second concerns the reason the slab always enters a multi-solution regime just before the slab ends, even when the imposed column density is much lower than the possible maximum value.

We are going to address these issues using the “intermediate” solution models as an illustration. Let us consider a set of models with $\xi = 1000$. Figure 9 displays the variation in P_{rad} , $P_{\text{rad}}(\text{lines})$, and P_{gas} along the slab for three values of the column density. We can see that the dependence of P_{rad} – and therefore also of P_{gas} , since the sum of P_{rad} and P_{gas} is constant – on the gas position inside the slab is almost the same for the three different

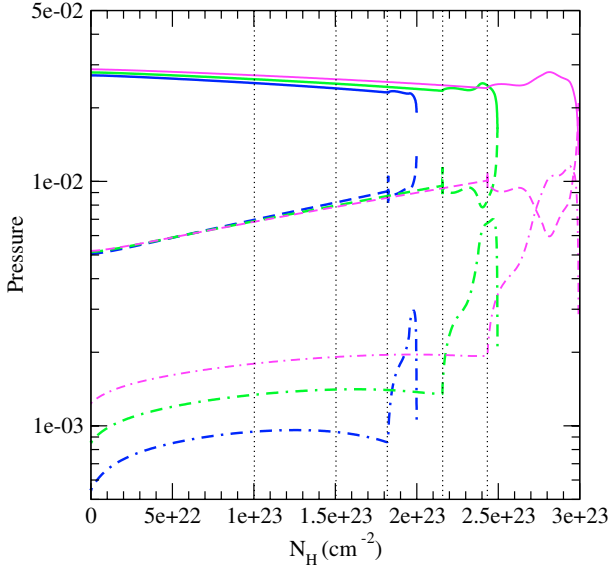


Fig. 9. Figure showing the variation of P_{rad} , $P_{\text{rad}}(\text{lines})$, and P_{gas} versus the column density, for 3 “intermediate” models of different thickness (MI 1, MI 2, and MI 3). P_{rad} is represented by solid lines, P_{gas} by dashed lines, and $P_{\text{rad}}(\text{lines})$ by dashed-dotted lines. The thin dotted vertical lines represent layers at different depths in the slab, corresponding namely to $1 \times 10^{23} \text{ cm}^{-2}$, $1.5 \times 10^{23} \text{ cm}^{-2}$, and to the first temperature jump in each model (1.82×10^{23} , 2.16×10^{23} , and $2.43 \times 10^{23} \text{ cm}^{-2}$ for the MI 1, MI 2, and MI 3 model, respectively).

thicknesses until the first temperature jump occurs. For the sake of simplicity, we do not show $P_{\text{rad}}/P_{\text{gas}}$ here, but it is clear that this ratio always displays approximately the same value (~ 2.5) at the temperature jump (the position of the temperature jump can be seen in Fig. 6, middle panel). Such temperature changes are accompanied by a strong increase in $P_{\text{rad}}(\text{lines})$. The thicker the slab, the larger the cold zone, and the stronger the increase in $P_{\text{rad}}(\text{lines})$. One can even observe an inversion of the gas pressure variation near the *back surface of the slab*, for the thickest case (MI 3 model). Very close to the back surface, the layers are optically thin for the continuum and the lines, which can thus escape from the medium. This induces a rapid decrease in the radiation pressure, as observed in the figure, and leads to a strong cooling that causes a rapid decrease in the temperature near the back surface of the slab. These coupled phenomena give an answer to the first problem.

The second issue is subtler. From Fig. 9 we know that P_{rad} decreases inside the slab (except near the back side, owing to the lines, as explained). Since P_{rad} is slightly larger in thicker slabs, the length traversed before reaching the ratio $P_{\text{rad}}/P_{\text{gas}}$ required for the temperature jump is larger for thicker slabs. However, this is not sufficient to explain why the temperature transition is located closer to the illuminated surface in thinner slabs, or the difference between the transition positions would not be so large in media with different thicknesses. Additional explanation can be found in Fig. 10, which compares the $P_{\text{rad}}/P_{\text{gas}}$ ratio versus the position in the slab (given in terms of column density) for the same three slab thicknesses as were discussed in the previous figure. This ratio decreases as we penetrate in the gas slab until it reaches a value ~ 2.5 , coinciding with a temperature jump. The figure shows that this ratio decreases more rapidly for the thinner (i.e. shorter), than for the thicker (longer) gas slab.

The explanation for this behavior can be found in the comparison between the spectral distribution of the first layer and of a layer located close to the place where the jump in

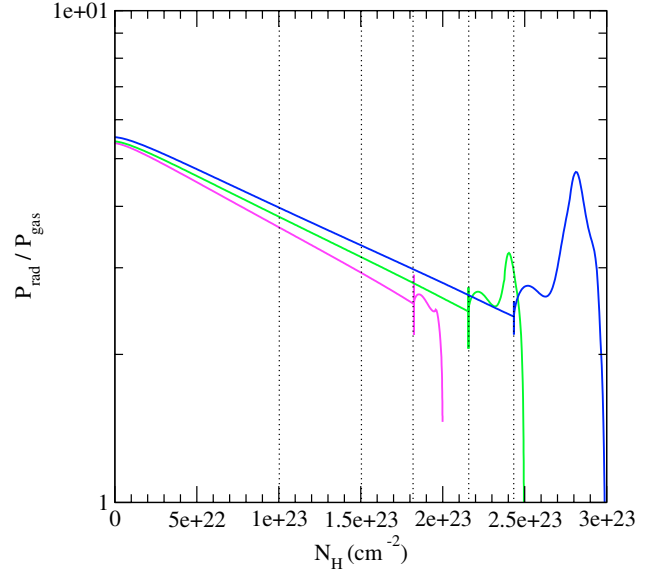


Fig. 10. Figure showing the $P_{\text{rad}}/P_{\text{gas}}$ ratio versus the column density, for the 3 “intermediate” models discussed in the previous figure. The thin dotted vertical lines represent layers at different depths in the slab (same as in Fig. 9).

temperature occurs. Figure 11 displays the spectral distribution of the mean intensity (again, the lines were suppressed for clarity), for two MI, “intermediate” models with total column densities $2 \times 10^{23} \text{ cm}^{-2}$ (left-hand panel) and $3 \times 10^{23} \text{ cm}^{-2}$ (right-hand panel), at different positions in the slab (from top to bottom: at the illuminated surface, at $1 \times 10^{23} \text{ cm}^{-2}$, $1.5 \times 10^{23} \text{ cm}^{-2}$, and at the first temperature jump – 1.82×10^{23} for MI 1 and 2.43×10^{23} for MI 3). We can observe that the spectral distribution of the continuum varies differently in the two media: at the same location in the slab, the spectrum is less absorbed in the thicker slab (right-hand panel), owing to the larger re-emission component. In other words, the spectral distribution of the thinner, shorter slab (left-hand panel) has a stronger trough, and reaches the multi-solution regime more rapidly, as explained above (cf. Fig. 2).

5. Observational implications

5.1. Outward emitted and absorbed spectra

Unfortunately, it is impossible to know what solution the plasma will adopt when attaining the multi-solution regime. For instance, it can oscillate between the hot and cold solutions, it can fragment into hot and cold clumps that will coexist, or it can take the form of a hot, dilute medium confining cold, denser clumps (the hot and cold media sharing the same pressure). We recall that the “cold” and “hot” models computed by TITAN can be interpreted as “extreme” models, as they adopt the “cold” or the “hot” solutions *throughout the slab*. The spectra emitted or absorbed by a given ionized medium, consisting of a mixture of gas in the hot and cold phases, should thus be intermediate between those resulting from the pure “cold” and “hot” models. The differences between the emitted and absorbed spectra obtained with the stable solutions can thus provide an indication of the maximum “error bars” associated to the spectra computed with the “intermediate” solution.

As an example, Figs. 12 and 13 give the pure absorption (top panels) and outward emission (bottom panels) spectra resulting from the “cold”, “hot”, and “intermediate” solutions for the MI 2

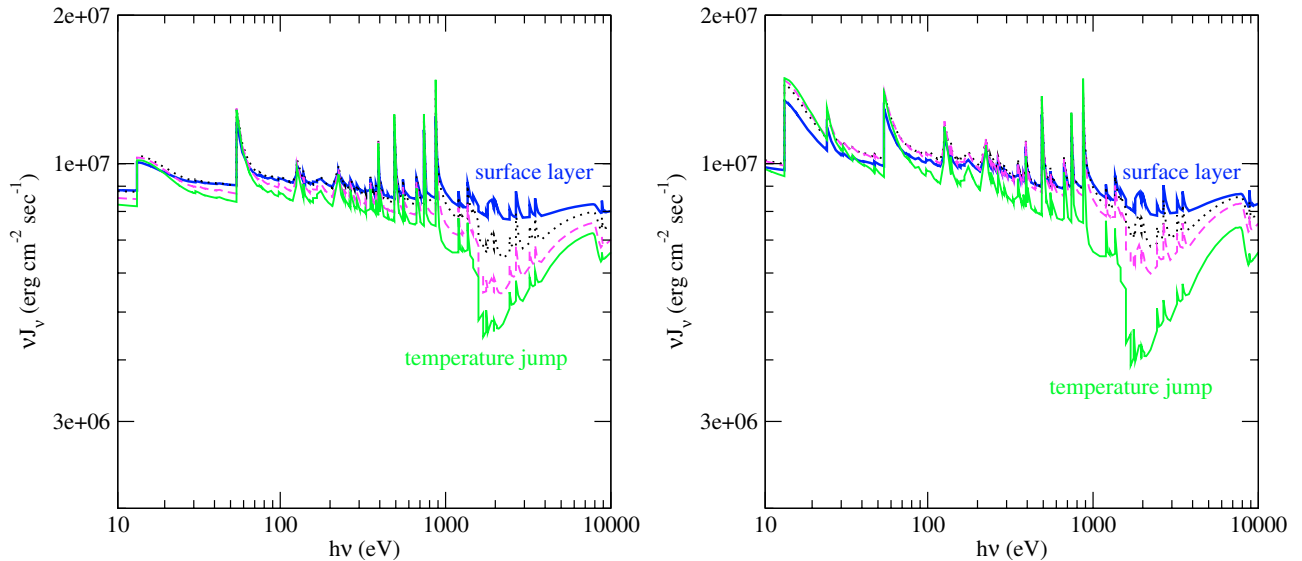


Fig. 11. Figure showing the medium intensity spectral distribution for two MI “intermediate” models with different column densities: on the *left-hand panel*, the thinner (shorter) model with $N_{\text{H}} = 2 \times 10^{23}$; on the *right-hand panel*, the thicker (longer) model with $N_{\text{H}} = 3 \times 10^{23}$. Both panels display the spectral distribution corresponding to 4 layers, from the illuminated surface of the slab (top curves) to the layer closer to the temperature jump (bottom curves).

and LI 1 models, respectively (see Fig. 6 for the corresponding temperature profiles). The spectra are represented with a resolution of 300 and have been displayed in two energy ranges: $10\text{--}10^4$ eV (left-hand panels), with a zoom in the $700\text{--}1200$ eV region (right-hand panel) to more clearly observe the differences. The lower solid lines correspond to the “cold” models, the middle lines to the “intermediate” models, and the upper lines to the “hot” models. The incident ionizing continuum and the spectrum corresponding to the half-sum of the “cold” and “hot” models are also plotted, for comparison. The outward emission spectrum has been computed for an opening angle of 45 degrees that, according to the unified scheme of AGN (Antonucci & Miller 1985), is in agreement with the expected geometry for the warm absorber in Seyfert 1 nuclei or the emissive region in Seyfert 2 s.

Investigating the MI 2 spectra in Fig. 12, we can see that the “intermediate” model spectra is extraordinarily close to the half-sum of the “cold” and “hot” spectra, though these ones are quite different. The differences amount at most to 1 or 2% for the outward emitted spectrum and to 20% for the absorption spectrum. The agreement is not as good for the second case (LI 1 model, Fig. 13), where the differences between the “intermediate” model and the half-sum of the “cold” and “hot” models typically amount to a factor 2 for the absorption spectrum. The agreement is much better for the outward emission in the X-ray range. This is due to the strong imprint of the cold layers near the back surface of the “cold” model, which absorb the UV-X spectrum almost completely. In contrast, the X-ray outward emission, being due mainly to the deep layers, is not very different for the “hot” and the “cold” models.

We observe that the lines have similar intensities in the “cold” and “hot” spectra, and also in the “intermediate” and half-sum spectra, which happens in spite of large differences in the continuum intensity, in particular for the ionization edges. Such behavior is due to the main lines being saturated resonance transitions, while the ionization edges are optically thinner, and therefore almost proportional to the thickness of the region containing the emitting ion (apart from the diffuse emission contribution).

5.2. Ionization states

Differences in the ionization state for “hot” and “cold” models are illustrated by Fig. 14, which displays the fractional ionization of two important elements – Si (top panels) and O (bottom panels) – for the “cold” (left-hand panels) and “hot” (right-hand panels) models already depicted in Fig. 12. When observing Fig. 14, we understand why the intensities of the ionization edges are different in “cold” and “hot” models. This happens because the regions producing the various ions are very different in the two models; for instance, the length of the O VII and O VIII regions is about three times larger in the “cold” model than in the “hot” model, these differences being somewhat larger than the discrepancy in the corresponding spectra.

5.3. Variability

In the multi-solution regime, the medium should be made of a mixture of gas in the hot and cold phases, and the relative proportion of those phases could be varying with time. The whole medium should thus oscillate between physical states located somewhere in the parameters’ region covered by the “hot” and “cold” models. The variation timescale in such a medium is basically the thermal time in the multi-branch region. However, if the medium is subject to a change in temperature, this will not necessarily be immediately followed by a change in ionization that induces modifications in the main absorbing or emitting ions. It all depends on the relative values of the thermal time t_{th} , the ionization time t_{ion} , and the recombination time t_{rec} . One thus expects two types of variability: a relatively weak variability related only to a temperature variation and a stronger variability related to a change in ionization state. If t_{ion} or t_{rec} are smaller than t_{th} , strong variations in the emitted/absorbed spectrum should be observed during the thermal time-scale, with the main emission/absorption lines and ionization edges being replaced by lines and edges of other ions. If t_{ion} and t_{rec} are larger than t_{th} , the spectrum should display smaller changes, like a simple variation in the relative intensity of the spectral features.

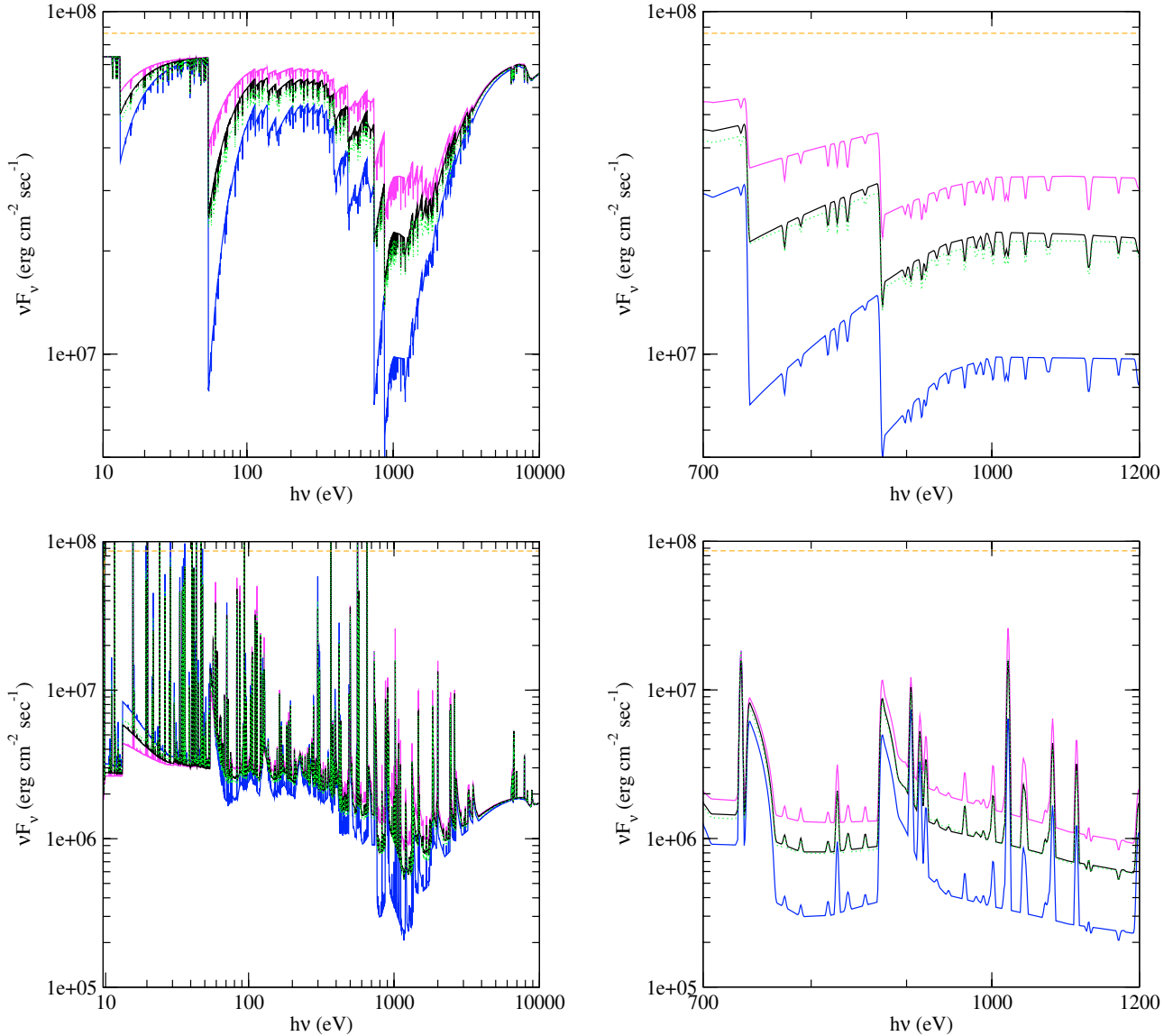


Fig. 12. The pure absorption (*top panels*) and outward emission spectra (*bottom panels*) for the MI 1 model. The “cold” solution model is represented by the lower blue lines, the “hot” model by upper magenta lines, and the “intermediate” model by the middle black lines; the spectra corresponding to the half-sum of the “hot” and “cold” models are also plotted for comparison (green dotted lines). The orange dashed line corresponds to the incident ionizing continuum. The spectra are represented with a resolution of 300; the *right-hand panel* focuses on the 700–1200 eV energy range for details, while the *left-hand panel* shows a larger band covering the 10–10⁴ eV range. Notice the excellent agreement between the “intermediate” and half-sum spectra over the entire energy range.

Let us compare these three timescales. The thermal time t_{th} is on the order of $kT/n\Lambda$. In the multi-solution regime, the cooling and the heating are dominated by atomic processes, and Λ is on the order of 10^{-23} erg cm³ s⁻¹, so t_{th} writes as

$$t_{\text{th}} \sim \frac{T_5}{n_{12} \Lambda_{23}} \quad (\text{in units of s}), \quad (4)$$

where n_{12} is the density expressed in 10^{12} cm⁻³, Λ_{23} is the cooling function in 10^{-23} erg cm³ s⁻¹, and T_5 is the temperature in 10^5 K.

For a given ion, t_{rec} is equal to $t_{\text{rec}} = 1/(n_e \alpha_{\text{ion}})$ where n_e is the electron numerical density (roughly equal to the total density n), and α_{ion} the recombination coefficient of the given ion, including dielectronic recombinations. This coefficient is almost independent of the radiation flux, with a typical value of

10^{-11} cm³ s⁻¹ at the temperature of the multi-branch region for a heavy, highly ionized element, so t_{rec} writes as

$$t_{\text{rec}} \sim \frac{0.1}{n_{12} \alpha_{11}} \quad (\text{in units of s}), \quad (5)$$

where the recombination coefficient α_{11} is expressed in 10^{-11} cm³ s⁻¹. Thus, the recombination time t_{rec} of a heavy element in a highly ionized state is shorter than, or very close to, the thermal time t_{th} . One deduces that a thermal variation almost immediately induces a change in the ionization state.

Ionization equilibrium is reached after a time equal to the maximum time-scales given by t_{ion} and t_{rec} . The ionization time t_{ion} is defined as

$$t_{\text{ion}} = \left(\int_{\nu(\text{ion})}^{\nu(\text{max})} 4\pi \frac{J_\nu}{h\nu} \sigma_\nu d\nu \right)^{-1}, \quad (6)$$

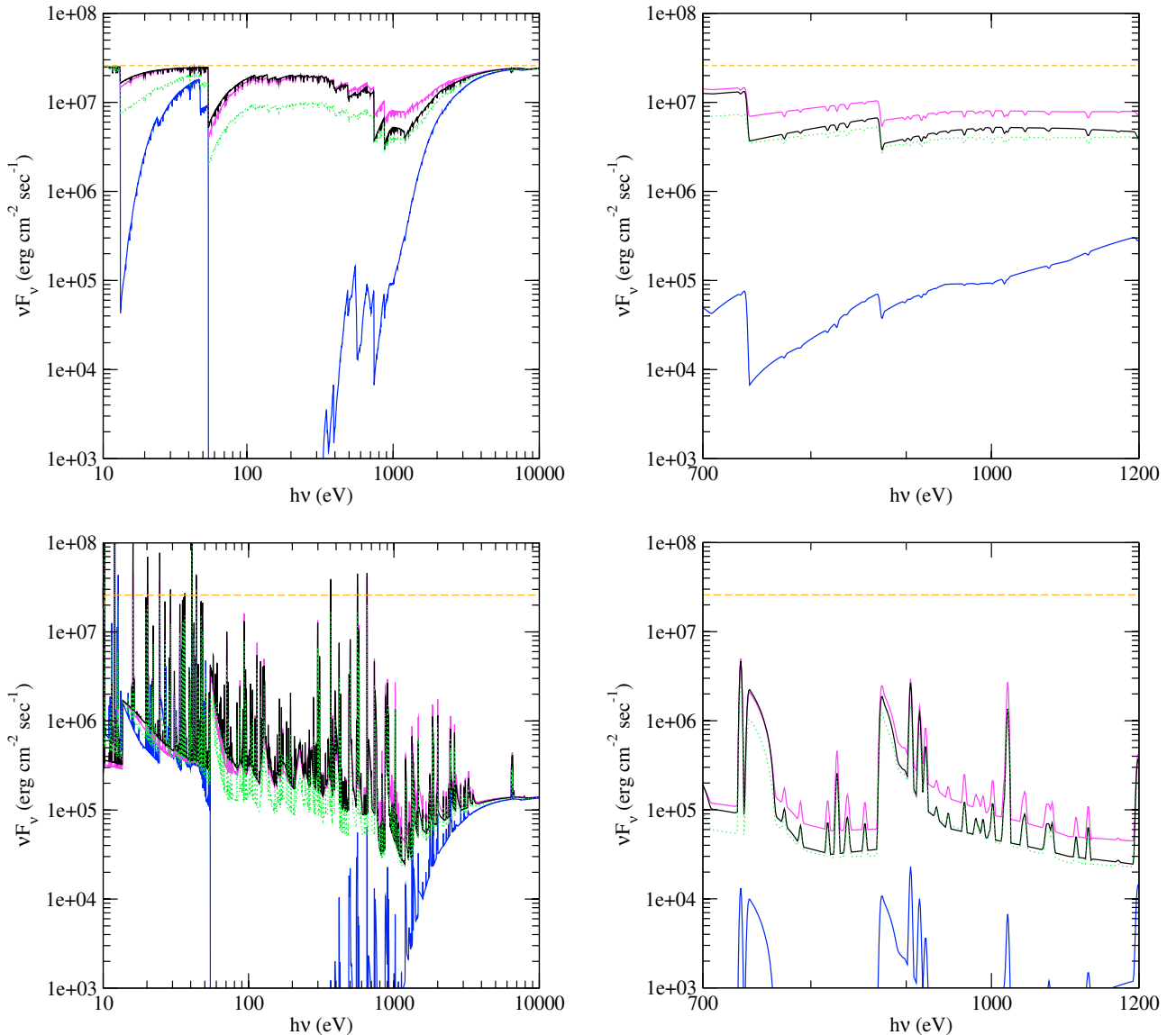


Fig. 13. Same as in the previous figure, only for the lower ionization model LI1. In this case, the agreement between the “intermediate” and half-sum spectra is not as good as for the MI1 model. The differences are not so great for the outward emission in the X-ray range.

where σ_ν is the frequency-dependent photoionization cross-section of the given ion. As seen, J_ν varies across the slab, but we can make a very rough estimation of t_{ion} by assuming that J_ν is on the order of the incident flux, $F_\nu/2\pi$. This could lead to a large overestimation of the ionization rate and, therefore, to an underestimation of the ionization time, as J_ν is actually smaller than $F_\nu/2\pi$ in the deep layers at the back of the slab (cf. the outward emitted spectrum in Figs. 12 and 13). With our power-law incident spectrum described by $F_\nu \propto \nu^{-1}$ in the $10\text{--}10^{-5}$ eV range, and also assuming that the cross-section is proportional to ν^{-3} , one finds⁶

$$t_{\text{ion}} \sim \frac{3 \times 10^{-5}}{\xi_3 n_{12} \sigma_{19}} \quad (\text{in units of s}), \quad (7)$$

where ξ_3 is the ionization parameter ξ expressed in $10^3 \text{ erg cm s}^{-1}$ and σ_{19} is the cross-section at the ionization edge of the given ion expressed in 10^{-19} cm^2 .

⁶ To derive this equation, we have made use of the definition of ξ given in Eq. (3).

In conclusion, even if it may be underestimated by two orders of magnitude, t_{ion} is smaller than t_{rec} , and both time-scales are smaller than t_{th} . Therefore, if the temperature changes locally in the multi-branch region, a new ionization equilibrium settles in immediately.

The problem is more complex in practice. Indeed, in order to observe variations in the spectrum, the change of temperature should affect a large proportion of the multi-branch region. The mass fractions of the hot and cold phases are most probably within the same order of magnitude, so this zone should be made of cold, dense clumps embedded in a hotter and more dilute medium. In this case, the evaporation time of the clumps should govern the structural changes. This time-scale is close to the cold phase dynamical time, if evaporation is not saturated.

The dynamical time is roughly equal to $\Delta H/c_s$, where ΔH is the thickness of the multi-branch region, and c_s is the sound velocity in the cold phase. The sound velocity includes the radiation pressure, but in a proportion that depends on the relation between the radiation field and the gas. Since the multi-branch region is not very optically thick, one can neglect the radiation

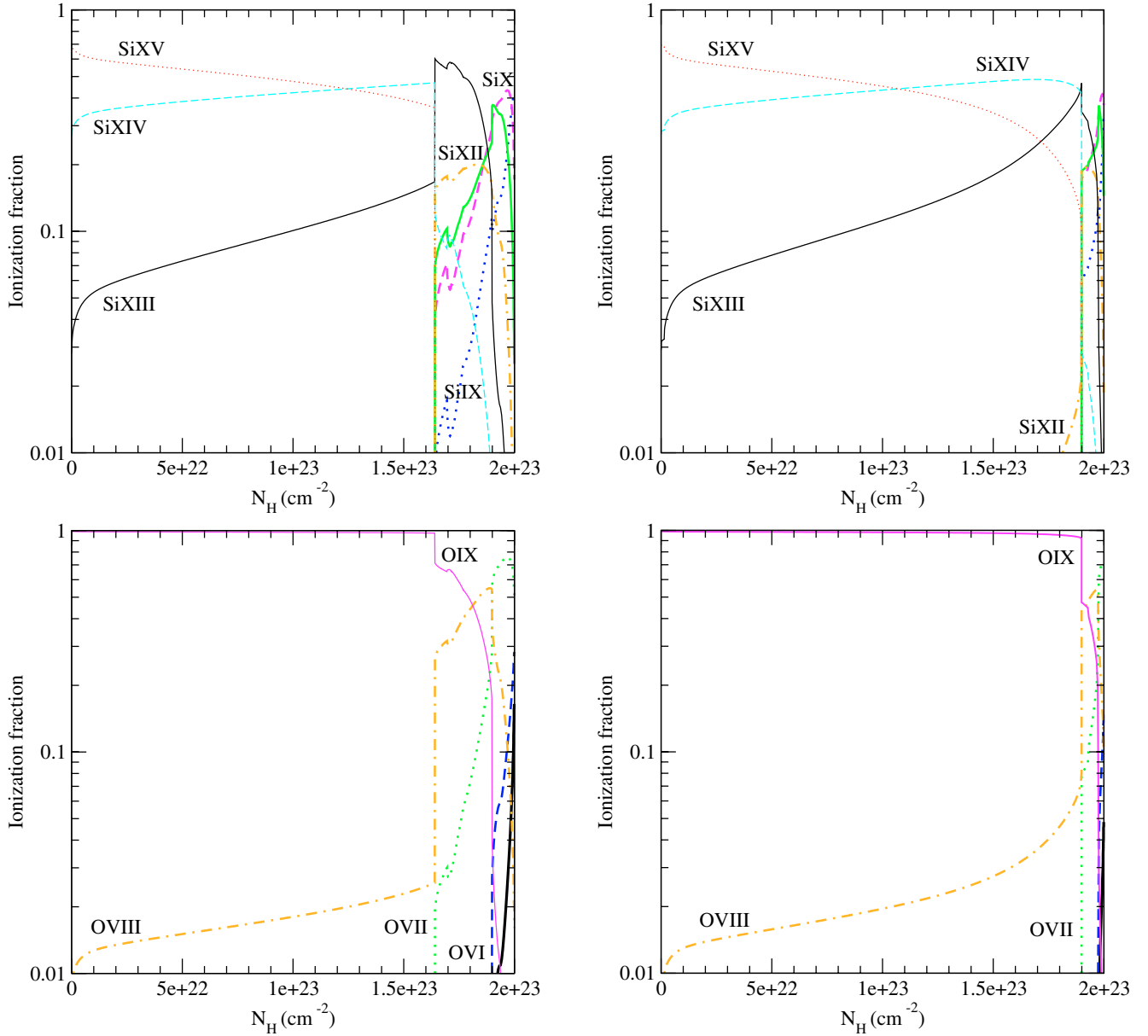


Fig. 14. The fractional ionization of the Si ions (*top panels*) and O ions (*bottom panels*) for the same models as in Fig. 12. The “cold” and “hot” models are displayed in the *left-hand* and *right-hand panels*, respectively.

pressure and simply assume $c_s = \sqrt{2kT/m_H}$, where m_H is the proton mass. The thickness of the multi-branch region is a fraction f_{multi} of the total thickness of the slab, which itself depends on the density (since the column density is a given parameter). Expressing the total column density in 10^{23} cm^{-2} , one finds

$$t_{\text{dyn}} \sim 2 \times 10^4 \frac{f_{\text{multi}} N_{23}}{\sqrt{T_5 n_{12}}} \quad (\text{in units of s}). \quad (8)$$

It is interesting to note that all timescales depend in the same way on the density, which is often an unknown parameter when dealing with observational data (e.g., warm absorber gas). If the timescales vary for different locations in the slab (because the density value is not the same at different depths), their ratio does not change much. In particular, the ratio $t_{\text{dyn}}/t_{\text{th}}$ is very large (on the order of 10^3 if the thermal instability affects 10% of the slab), therefore the multi-branch region should contain local thermal perturbations out of pressure equilibrium.

Chevallier et al. (2007) made a detailed study of the viability of pressure equilibrium media in the presence of variations in the incident radiation flux. The authors have shown that, although the global pressure equilibrium is generally preserved (with the medium responding to the variations by rapidly adjusting its ionization and thermal equilibrium), supersonic velocities develop in the gas, owing to local over- or under-pressure states. The same phenomenon should occur in the multi-branch region of our media, even in the absence of incident flux variations. To attack this problem, a complete perturbational study should be performed around the equilibrium state of the gas slab, but such a study is beyond the scope of the present paper. For the time being, we can just conclude that large spectral fluctuations corresponding to the onset of a “cold” or a “hot” solution could be observed in timescales on the order of the dynamical time, independently of any variation in the radiation field external to the medium. Moreover, a strong turbulence implying supersonic velocities leading to line broadening should permanently exist in

the multi-branch region of thick, stratified, pressure equilibrium media.

5.4. Practical considerations

An important point to take into account when choosing which computational method to apply is that the full computation of the “hot” and “cold” models described here is extremely time-consuming, because the process is strongly unstable and requires thus more iterations than the isodensity scheme models. Given the results presented in this paper, it seems reasonable to use the simpler, isodensity scheme to compute constant pressure models or hydrostatic equilibrium models. This procedure is less ad-hoc than arbitrarily choosing between one of the possible solutions resulting, in the end, in gas structures and emitted/absorbed spectra very close to what is expected from an ionized medium consisting in similar proportions of gas in the hot and cold phases.

6. Conclusions

1. We have addressed the thermal instability issue in the case of optically thick, stratified media in total pressure equilibrium.
2. In order to do that, we have developed and implemented a new algorithm in the TITAN code; this algorithm, based on an isobaric computational method, selects the hot/cold stable solution and computes a fully consistent photoionized model for each solution.
3. We chose to work with a few models that encompass the range of conditions valid for the warm absorber in AGN; our results can be applied to media in any pressure equilibrium condition, e.g., constant gas pressure, constant total pressure, or hydrostatic pressure equilibrium.
4. We have shown that a thick, stratified medium ionized by X-rays behaves differently from a thin ionized medium. This happens mainly for two reasons: first, the spectral distribution of the mean intensity at the illuminated surface of the slab is different from the incident spectrum, as it equally contains a “returning” radiation component emitted by the slab itself; second, the spectral distribution changes as the radiation progresses inside the medium and, as a consequence, the shape of the S-curve also changes. These effects depend on the thickness of the medium and on its ionization.
5. This has observational implications in the emitted/absorbed spectra, ionization states, and variability. It is impossible to know what solution the plasma will adopt when attaining the multi-solution regime: it can oscillate between the hot and cold solutions, it can fragment into hot and cold clumps that will coexist, or it can take the form of a hot, dilute medium confining cold, denser clumps. Nevertheless, one expects the emitted/absorbed spectrum to be intermediate between those resulting from pure cold and hot models.
6. We have compared the results obtained with models based on the pure hot/cold solution and models computed with an approximate, intermediate solution. We demonstrate that the pure hot/cold models represent two extreme results corresponding to a given gas composition and photoionizing flux, being compatible with the two stable solutions. The three (hot, cold, and intermediate) models differ not only in

the layers where multiple solutions are possible, but throughout the gas slab, because the entire radiation field suffers modifications while crossing a thick medium.

7. The spectra emitted or absorbed by a given ionized medium, consisting of a mixture of gas in the hot and cold phases, should thus be intermediate between those resulting from the pure cold and hot models; therefore, the intermediate model provides a good description of such a mixed-phase medium. The differences between the emitted and absorbed spectra obtained with the stable solutions indicate the maximum “error bars” associated to the spectra computed with the “intermediate” solution.
8. The relative proportion of the hot and cold phases could vary with time. One expects two types of variability: a relatively weak variability related only to a temperature variation and a stronger variability related to a change of ionization state. Large spectral fluctuations corresponding to the onset of a cold/hot solution could be observed in timescales on the order of the dynamical time. Moreover, a strong turbulence implying supersonic velocities leading to line broadening should permanently exist in the multi-branch region of thick, stratified, pressure equilibrium media.

Acknowledgements. We acknowledge grant BPD/11641/2002 of the FCT, Portugal, grant 1P03 D00829 of the PSCSR, Poland, and support from LEA and astro-PF, Poland-France. The authors thank B. Czerny and A. Różańska for fruitful discussions on the subjects of thermal instability and electron conductivity.

References

- Allen, C. W. 1973, *Astrophysical Quantities* (U. London, Athlone Press)
- Antonucci, R. R. J., & Miller, J. S. 1985, *ApJ*, 297, 621
- Ballantyne, D. R., Ross, R. R., & Fabian, A. C. 2001, *MNRAS*, 327, 10
- Begelman, M. C., & McKee, C. F. 1990, *ApJ*, 358, 375
- Chevallier, L., Collin, S., Dumont, A.-M., et al. 2006, *A&A*, 449, 493
- Chevallier, L., Czerny, B., Różańska, A., & Gonçalves 2007, *A&A*, in press [astro-ph/0701112]
- Chevallier, L., et al., in preparation
- Collin, S., Dumont, A.-M., & Godet, O. 2004, *A&A*, 419, 877
- Collin-Souffrin, S., & Dumont, S. 1986, *A&A*, 166, 13
- Dumont, A.-M., Abrassart, A., & Collin, S. 2000, *A&A*, 357, 823
- Dumont, A.-M., & Collin, S. 2001, *Spectroscopic Challenges of Photoionized Plasmas*, ASP Conf. Ser., 247, 231
- Dumont, A.-M., Czerny, B., Collin, S., & Zycy, P. T. 2002, *A&A*, 387, 63
- Dumont, A.-M., Collin, S., Paletou, F., et al. 2003, *A&A*, 407, 13
- Ferland, G. J., Korista, K. T., Verner, D. A., et al. 1998, *PASP*, 100, 761
- Field, G. B. 1965, *ApJ*, 142, 531
- Field, G. B., Goldsmith, D. W., & Habing, H. J. 1969, *ApJ*, 155, L149
- Gonçalves, A. C., & Soria, R. 2006, *MNRAS*, 371, 673
- Gonçalves, A. C., Collin, S., Dumont, A.-M., et al. 2006, *A&A*, 451, L23
- Kallman, T., & Bautista, M. 2001, *ApJS*, 133, 221
- Kallman, T. R., & Krolik, J. H. 1995, *XSTAR*, a Spectral Analysis Tool, Users Guide, HEASARC (NASA/GSFC, Greenbelt)
- Kawaguchi, T., Shimura, T., & Mineshige, S. 2001, *ApJ*, 546, 966
- Ko, Y.-K., & Kallman, T. R. 1994, *ApJ*, 431, 273
- Krolik, J. H., McKee, C. F., & Tarter, C. B. 1981, *ApJ*, 249, 422
- Madej, J., & Różańska, A. 2000, *A&A*, 356, 654
- McKee, C. F., & Begelman, M. C. 1990, *ApJ*, 358, 392
- Netzer, H. 1993, *ApJ*, 411, 594
- Netzer, H. 1996, *ApJ*, 473, 781
- Raymond, J. C. 1993, *ApJ*, 412, 267
- Różańska, A. 1999, *MNRAS*, 308, 751
- Różańska, A., & Czerny, B. 2000, *MNRAS*, 316, 473
- Różańska, A., Czerny, B., Dumont, A.-M., & Collin, S. 2002, *MNRAS*, 332, 799
- Różańska, A., Goosmann, R., Dumont, A.-M., & Czerny, B. 2006, *A&A*, 452, 1
- Shimura, T., Mineshige, S., & Takahara, F. 1995, *ApJ*, 439, 74